



ELSEVIER

Available online at www.sciencedirect.com

SCIENCE @ DIRECT®

Finite Elements in Analysis and Design 41 (2004) 147–171

FINITE ELEMENTS
IN ANALYSIS
AND DESIGN

www.elsevier.com/locate/finel

Stabilized conforming nodal integration: exactness and variational justification

K.Y. Sze^{a,*}, J.S. Chen^b, N. Sheng^a, X.H. Liu^a

^a*Department of Mechanical Engineering, The University of Hong Kong, Pokfulam Road, Hong Kong SAR, PR China*

^b*Department of Civil & Environmental Engineering, University of California, Los Angeles, 5713G Boelter Hall, CA 90095-1593, USA*

Received 16 December 2003; accepted 3 May 2004

Available online 5 August 2004

Abstract

In most Galerkin mesh-free methods, background integration cells partitioning the problem domain are required to evaluate the weak form. It is therefore worthwhile to consider these methods using the notions of domain decomposition with the integration cells being the subdomains. Presuming that the analytical solution is admissible in the trial solution, domain and boundary integration exactness, which depend on the orders of the employed trial solution and the required solution exactness, are identified for the strict satisfaction of traction reciprocity and natural boundary condition in the weak form. Unfortunately, trial solutions constructed by many mesh-free approximants contain non-polynomial terms which cannot be exactly integrated by Gaussian quadratures. Recently, stabilized conforming (SC) nodal integration for Galerkin mesh-free methods was proposed and illustrated to be linearly exact. This paper will discuss how linear exactness is ensured and how spurious oscillation encountered by direct nodal integration is suppressed in SC nodal integration from a domain decomposition point of view. Moreover, it will be shown that SC nodal integration can be formulated by the Hellinger–Reissner Principle and thus justified in the classical variational sense. Applications of the method to straight beam, plate and curved beam problems are presented.

© 2004 Elsevier B.V. All rights reserved.

Keywords: Mesh-free; Nodal integration; Integration; Galerkin; Hybrid-stress; Stabilized conforming

* Corresponding author. Tel.: +852-2859-2637; fax: +852-2858-5415.

E-mail address: kysze@hku.hk (K.Y. Sze).

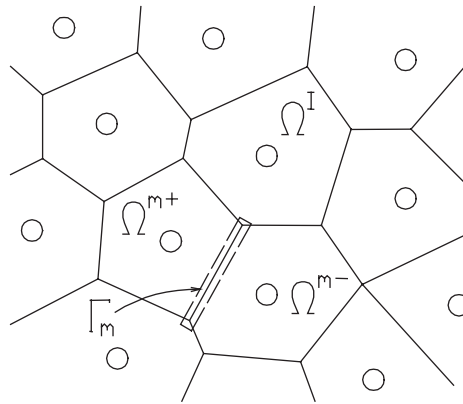


Fig. 1. In nodal integration for mesh-free methods, Voronoi cells can be the nodal subdomains. The representative points in the cells are nodes O . Γ_m denotes the common boundary segment of subdomains Ω^{m+} and Ω^{m-} .

1. Introduction

Mesh-free methods have been very actively pursued by the research community of computational mechanics in the last decade. Broadly speaking, mesh-free methods can be categorized into Galerkin mesh-free methods [1–5], Petrov–Galerkin mesh-free methods [6] and collocation mesh-free methods [7–9]. As integration of the weak form is necessary in Galerkin mesh-free methods, background integration cells are required. It is worthwhile to consider these methods using the notion of domain decomposition with the integration cells viewed as the subdomains partitioning the domain. Presuming that the analytical solution is admissible in the trial solution, the mechanism that the Galerkin method reproduces the analytical solution is studied. Though the weak form does not need to be integrated exactly, certain domain and boundary integration exactness requirements that depend on the orders of the trial solution and the desired order of solution exactness are identified for the strict fulfillment of the traction reciprocity and the natural boundary condition in the weak form. Unfortunately, commonly-used mesh-free approximants including those constructed by moving least squares and reproducing kernel particle methods [2,3] contain non-polynomial components which cannot be exactly integrated by Gaussian quadratures.

To reduce the effort on defining the integration cells, large rectangular and triangular cells and high-order quadratures are normally employed. The practice becomes cumbersome if the domain boundary is not straight. An alternative way to evaluate the weak form is the nodal integration whose core idea is to use nodes as the integration sampling points. By using the nodes as the representative points in Dirichlet tessellation, which is an “equal-distant rule” (see Fig. 1), the nodal subdomains are the Voronoi cells [10]. Though the system matrix is non-singular, numerical solutions obtained by this “direct nodal integration” may be plagued by spurious oscillation which also occurs in the finite difference method. This phenomenon is often explained by the observation that the nodal gradient is independent of the nodal parameters at the same node. Beissel and Belytschko stabilized the oscillation by penalizing the weak form with the square of the equilibrium residue [11]. The same stabilized nodal integration was later employed by Bonet and Kulasegaram [12] who adopted the smoothed particle hydrodynamics approximation. Nevertheless, the equilibrium residual involves the second derivatives which are rather expensive to compute.

Instead of using the nodal gradient to compute the weak form of the nodal subdomains, Chen and his coworkers recently employed the smoothed nodal gradient [13–15] which, via the divergence theorem, is evaluated by boundary integration. In this manner, the trial solution needs to be evaluated on the boundary of the nodal subdomains only. The whole formulation does not involve any derivatives of the trial solution. Furthermore, the nodal integration can yield linear exactness and the oscillation occurring in the direct nodal integration is not observed. For the above reasons, the former integration scheme is termed the stabilized conforming (SC) nodal integration.

The paper is organized as follows. Section 2 presents two sufficient conditions for securing the solution exactness in Galerkin domain decomposition method. Section 3 briefly introduces the direct and stabilized nodal integrations. Section 4 presents how linear exactness is secured in the SC nodal integration. Interestingly, the conditions identified in Section 2 are not required in the SC nodal integration and only a much less demanding boundary integration consistency is necessary. Section 5 points out that the SC integration method can be formulated by the Hellinger–Reissner Principle and thus justified in the classical variational sense. Section 6 presents the numerical results for some one-dimensional, straight beam, plate and curved beam problems.

2. Domain decomposition and integration exactness

The terms “meshless”, “mesh-free” and “element-free” generally refer to the ability of constructing approximations or interpolations without referring to meshes. They stand a sharp contrast to finite element method whose trial solution quality is very sensitive to the mesh regularity. Nevertheless, Galerkin mesh-free methods often require a background mesh or integration subdomains for evaluating the domain integrals appearing in the weak form. In a broad sense, domain decomposition is involved. It is therefore worthwhile to examine Galerkin mesh-free methods by the concepts of domain decomposition. The two-dimensional elasticity problem is selected to be the subject of discussion.

The two-dimensional domain under consideration and its entire boundary are denoted by Ω and $\partial\Omega$, respectively. Moreover, $\partial\Omega = \Gamma_u \cup \Gamma_t$ and $\Gamma_u \cap \Gamma_t = \text{null}$ where Γ_u and Γ_t are prescribed with the essential boundary condition (e.b.c.) and the natural boundary condition (n.b.c.). Ω is partitioned into subdomains Ω^e 's such that $\bigcup_e \Omega^e = \Omega$ and $\Omega^a \cap \Omega^b = \text{null}$ for $a \neq b$. With displacement $\mathbf{u} = \{u_1, u_2\}^T$ taken to be the only field variable whereas displacement compatibility and e.b.c. taken to be prerequisites, the strong form of the domain decomposition problem can be summarized as

$$\text{equilibrium condition: } \mathbf{L}^T \mathbf{C}(\mathbf{L}\mathbf{u}) + \bar{\mathbf{b}} = \mathbf{0} \quad \text{in } \Omega^{e'}\text{s} \tag{1}$$

$$\text{n.b.c.: } \mathbf{nC}(\mathbf{L}\mathbf{u}) = \bar{\mathbf{t}} \quad \text{on all } \Gamma_t^{e'}\text{s } (\Gamma_t^e = \Gamma_t \cap \partial\Omega^e) \tag{2}$$

$$\text{traction reciprocity: } (\mathbf{nC}(\mathbf{L}\mathbf{u}))^{m+} + (\mathbf{nC}(\mathbf{L}\mathbf{u}))^{m-} = \mathbf{0} \quad \text{on all } \Gamma_m^e\text{s } (\Gamma_m = \partial\Omega^{m+} \cap \partial\Omega^{m-}) \tag{3}$$

where

$$\mathbf{L} = \begin{bmatrix} \partial/\partial x_1 & 0 \\ 0 & \partial/\partial x_2 \\ \partial/\partial x_2 & \partial/\partial x_1 \end{bmatrix}, \quad \mathbf{n} = \begin{bmatrix} n_1 & 0 & n_2 \\ 0 & n_2 & n_1 \end{bmatrix} \quad \text{and} \quad \begin{Bmatrix} n_1 \\ n_2 \end{Bmatrix}$$

is the boundary outward unit normal.

Moreover, \mathbf{C} is the material elasticity matrix, $\bar{\mathbf{b}}$ is the prescribed body force and $\bar{\mathbf{t}}$ is the prescribed boundary traction on Γ_t . Superscripts “ $m+$ ” and “ $m-$ ” designate any pair of adjacent subdomains and Γ_m denotes their common boundary segment as portrayed in Fig. 1. Imposition of the e.b.c., which can be stated as

$$\mathbf{u} = \bar{\mathbf{u}} \quad \text{on all } \Gamma_u^{e'} \text{ s } (\Gamma_u^e = \Gamma_u \cap \partial\Omega^e) \quad (4)$$

in mesh-free methods, is not as straight forward as in the finite element method but can always be done. Displacement compatibility requires

$$\mathbf{u}^{m+} = \mathbf{u}^{m-} \quad \text{on all } \Gamma_m' \text{ s.} \quad (5)$$

The trial solution can always be expressed as

$$\mathbf{u} = \mathbf{N}\mathbf{q}, \quad (6)$$

where \mathbf{N} is the shape function matrix and \mathbf{q} is the vector comprising all nodal parameters or d.o.f.s. The following potential energy functional can be adopted:

$$\Pi = \mathbf{q}^T \sum_e \left[\left\langle \frac{1}{2} (\mathbf{LN})^T \mathbf{C} (\mathbf{LN}) \mathbf{q} - \mathbf{N}^T \bar{\mathbf{b}} \right\rangle_{\Omega^e} - \langle \mathbf{N}^T \bar{\mathbf{t}} \rangle_{\Gamma_t^e} \right] \quad (7)$$

where $\langle \circ \rangle_{\Omega}$ and $\langle \circ \rangle_{\Gamma}$ denote the numerically integrated counterparts of the exact integrals $\int_{\Omega} \circ \, d\Omega$ and $\int_{\Gamma} \circ \, d\Gamma$, respectively. Variation of Π is

$$\delta\Pi = \delta\mathbf{q}^T \sum_e \left[\langle (\mathbf{LN})^T \mathbf{C} (\mathbf{LN}) \mathbf{q} - \mathbf{N}^T \bar{\mathbf{b}} \rangle_{\Omega^e} - \langle \mathbf{N}^T \bar{\mathbf{t}} \rangle_{\Gamma_t^e} \right]. \quad (8)$$

The subdomain boundary $\partial\Omega^e$ can be partitioned into Γ_u^e , Γ_t^e and the portion shared with the adjacent subdomains. Recalling that e.b.c. is a prerequisite (i.e. $\delta\mathbf{u} = \mathbf{0}$ on Γ_u^e), the divergence theorem can be written as

$$\langle (\mathbf{LN})^T \mathbf{C} (\mathbf{LN}) \rangle_{\Omega^e} = - \int_{\Omega^e} \mathbf{N}^T [\mathbf{L}^T \mathbf{C} (\mathbf{LN})] \, d\Omega + \int_{\partial\Omega^e / \Gamma_u^e} \mathbf{N}^T \mathbf{n} \mathbf{C} (\mathbf{LN}) \, d\Gamma + \mathbf{E}^e \quad (9)$$

in which \mathbf{E}^e is the error induced by the numerical integration and \int denotes the exact integration as previously specified. By virtue of (9), (8) can be written as

$$\begin{aligned} \delta\Pi_P = & \delta\mathbf{q}^T \sum_e \left(- \int_{\Omega^e} \mathbf{N}^T [\mathbf{L}^T \mathbf{C} (\mathbf{LN})] \, d\Omega \mathbf{q} - \langle \mathbf{N}^T \bar{\mathbf{b}} \rangle_{\Omega^e} \right. \\ & \left. + \int_{\Gamma_t^e} \mathbf{N}^T \mathbf{n} \mathbf{C} (\mathbf{LN}) \, d\Gamma \mathbf{q} - \langle \mathbf{N}^T \bar{\mathbf{t}} \rangle_{\Gamma_t^e} + \mathbf{E}^e \mathbf{q} \right) \\ & + \delta\mathbf{q}^T \sum_m \left(\int_{\Gamma_m} [\mathbf{N}^T \mathbf{n} \mathbf{C} (\mathbf{LN})]^{m+} \, d\Gamma + \int_{\Gamma_m} [\mathbf{N}^T \mathbf{n} \mathbf{C} (\mathbf{LN})]^{m-} \, d\Gamma \right) \mathbf{q}. \end{aligned} \quad (10)$$

If the analytical solution is admissible in the trial solution, one would expect that the former will be predicted by Galerkin methods. However, this may not be the case when numerical integration is employed. The most trivial way ensuring that the analytical solution can be reproduced is to evaluate all

terms in (7) exactly. Unfortunately, such quadratures, which are based on polynomial integrand, may not exist when the trial solution is based on mesh-free approximants. On the other hand, the integrands leading to the element stiffness matrices of distorted finite elements cannot be exactly integrated numerically due to the presence of the reciprocal of the Jacobian determinant as well. However, these elements pass the patch test and are linearly exact. In this light, exact integration of the weak form is not a necessity.

To examine the minimum quadrature for securing the k th order exactness, \mathbf{q} , $\bar{\mathbf{b}}$ and $\bar{\mathbf{t}}$ in δII_P are set to, respectively, $\tilde{\mathbf{q}}$, $\tilde{\mathbf{b}}$ and $\mathbf{nC}(\mathbf{LN})\tilde{\mathbf{q}}$ such that $\mathbf{u} = \mathbf{N}\tilde{\mathbf{q}}$ and $\bar{\mathbf{b}} = \tilde{\mathbf{b}}$ satisfy (1) whereas the order of \mathbf{u} is k . Thus,

$$\begin{aligned} \delta II_P|_{\mathbf{q}=\tilde{\mathbf{q}}, \bar{\mathbf{b}}=\tilde{\mathbf{b}}, \bar{\mathbf{t}}=\mathbf{n}\tilde{\sigma}} = & \delta \mathbf{q}^T \sum_e \left(- \int_{\Omega^e} \mathbf{N}^T (\mathbf{L}^T \tilde{\sigma}) \, d\Omega - \langle \mathbf{N}^T \tilde{\mathbf{b}} \rangle_{\Omega^e} \right. \\ & \left. + \int_{\Gamma_t^e} \mathbf{N}^T \mathbf{n} \tilde{\sigma} \, d\Gamma - \langle \mathbf{N}^T \mathbf{n} \tilde{\sigma} \rangle_{\Gamma_t^e} + \mathbf{E}^e \tilde{\mathbf{q}} \right) \end{aligned} \quad (11)$$

in which $\tilde{\sigma}$ denotes $\mathbf{C}(\mathbf{LN})\tilde{\mathbf{q}}$. As displacement compatibility is a prerequisite and “ \int ” denotes exact integration, the last summation term in (10) vanishes identically and disappears in (11). Provided that the system matrix is non-singular, the sufficient conditions for $\mathbf{q} = \tilde{\mathbf{q}}$, $\bar{\mathbf{b}} = \tilde{\mathbf{b}}$ and $\bar{\mathbf{t}} = \mathbf{n}\tilde{\sigma}$ as the unique solution of the weak form are:

- domain integration exactness (DIE): $\langle (\mathbf{LN})^T \tilde{\sigma} \rangle_{\Omega^e} = \int_{\Omega^e} (\mathbf{LN})^T \tilde{\sigma} \, d\Omega$,
- boundary integration exactness (BIE): $\langle \mathbf{N}^T \mathbf{n} \tilde{\sigma} \rangle_{\Gamma_t^e} = \int_{\Gamma_t^e} \mathbf{N}^T \mathbf{n} \tilde{\sigma} \, d\Gamma$.

It should be remarked that DIE implies $\mathbf{E}^e \tilde{\mathbf{q}}$ in (11) equal to zero. Since the order of $\mathbf{N}^T \tilde{\mathbf{b}}$ is always smaller than or equal to that of $(\mathbf{LN})^T \tilde{\sigma}$, DIE also ensures that the prescribed body force term is evaluated exactly and thus the pairwise cancellation of the two domain integration terms in (11). On the other hand, BIE leads to the pairwise cancellation of the boundary terms in (11).

Noticeably, a higher order trial displacement or, equivalently, its shape function matrix \mathbf{N} would require higher order quadrature rules to secure DIE and BIE regardless of how fine the integration subdomains are. Finally, the minimal quadrature for DIE and that for exact integration of $(\mathbf{LN})^T \mathbf{C}(\mathbf{LN})$ are different. The following examples illustrate the importance of DIE and BIE.

Example 2.1. To illustrate the importance of DIE, the following one-dimensional zero and constant body force problems are considered:

problem 1: $\frac{d^2 u}{dx^2} = 0$ for $0 \leq x \leq 6$, $u|_{x=0} = 0$, $\sigma|_{x=6} = 1 \Rightarrow u = x$ and $\sigma = 1$,

problem 2: $\frac{d^2 u}{dx^2} + 1 = 0$ for $0 \leq x \leq 6$, $u|_{x=0} = 0$, $\sigma|_{x=6} = 1 \Rightarrow u = -x^2/2 + 7x$
and $\sigma = -x + 7$,

where $\sigma = du/dx$. The following trial solutions that comprise the exact solutions and satisfy the e.b.c. are employed:

$$u_1^h = c_1 x + c_2 x^2, \quad u_2^h = c_1 x + c_2 x^2 + c_3 x^3 \quad \text{and} \quad u_3^h = c_1 x + c_2 x^2 + c_3 x^3 + c_4 x^4$$

Table 1
Predicted tip deflections and stresses for problem 1 by different integration schemes

Trial solution	Minimum quadrature order for DIE	Employed quadrature order	No. of integration subdomains	Total no. of integration points	$u^h _{x=6}$	$\frac{du^h}{dx} _{x=6}$
u_1^h	1	1	2	2	Exact	Exact
		1	3	3	6.1875	1.5938
u_2^h	2	1	12	12	6.0004	1.0180
		2	2	4	Exact	Exact
u_3^h	2	1	4	4	6.0417	1.2292
		1	12	12	6.0004	1.0180
		2	2	4	Exact	Exact

Table 2
Predicted tip deflections and stresses for problem 2 by different integration schemes

Trial solution	Minimum quadrature order for DIE	Employed quadrature order	No. of integration subdomains	Total no. of integration points	$u^h _{x=6}$	$\frac{du^h}{dx} _{x=6}$
u_1^h	2	1	2	2	Exact	-0.5000
		1	12	12	Exact	0.9685
		2	1	2	Exact	Exact
u_2^h	2	1	3	3	24.7500	2.8125
		1	12	12	24.0015	1.0407
		2	2	4	Exact	Exact
u_3^h	3	1	4	4	24.1667	-5.4114
		1	12	12	24.0015	0.8203
		2	2	4	Exact	-0.2500
		2	6	12	Exact	0.9954
		3	2	6	Exact	Exact

which require at least 2, 3 and 4 integration points to secure a non-singular system matrix, respectively. Given a quadrature rule, the above numbers of integration points are secured by partitioning the domain into equal-sized integration subdomains.

For problem 1, the orders of $(\mathbf{LN})^T \tilde{\sigma}$'s for u_1^h , u_2^h and u_3^h are, respectively, first, second and third. Hence, the minimal quadratures for DIE are, respectively, the first, second and second-order quadratures. For problem 2, the orders of $(\mathbf{LN})^T \tilde{\sigma}$'s for u_1^h , u_2^h and u_3^h are, respectively, second, third and fourth. Hence, the minimal quadratures for DIE are, respectively, the second, second and third-order quadratures. Tables 1 and 2 list the predicted u^h and stress at $x = 6$ for different combinations of quadrature and number of integration subdomains. Whenever the employed quadrature orders are lower than the minimal, it can

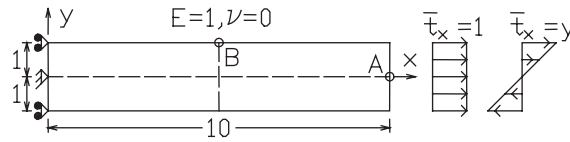


Fig. 2. A 10×2 rectangular panel divided into four integration subdomains.

Table 3
Predictions for problem 3 by using different quadratures to evaluate the work done

Trial solution	Minimum quadrature order for BIE	Employed quadrature order	$u_x^h _{x=10,y=0}$	$u_y^h _{x=10,y=0}$	$\frac{du_x^h}{dx} \Big _{x=5,y=1}$
\mathbf{u}_1^h	2	1	10.0343	Exact	0.9931
		2	Exact	Exact	Exact
		3	Exact	Exact	Exact
\mathbf{u}_2^h	2	1	10.0670	Exact	1.0079
		2	Exact	Exact	Exact
		3	Exact	Exact	Exact

be seen that the predictions are erroneous regardless of how many integration subdomains are used. The importance of DIE in securing linear and quadratic exactness is demonstrated.

Example 2.2. To illustrate the importance of BIE, the two-dimensional elasticity problems depicted in Fig. 2 are considered. The analytical solutions are:

- problem 3 ($\bar{t}_x|_{x=10} = 1$): $u_x = x, u_y = 0, \sigma_x = 1, \sigma_y = \tau_{xy} = 0,$
- problem 4 ($\bar{t}_x|_{x=10} = y$): $u_x = xy, u_y = -x^2/2, \sigma_x = y, \sigma_y = \tau_{xy} = 0.$

The following trial solutions are considered:

- $\mathbf{u}_1^h \sim$ complete biquadratic polynomial expansion with $u_x^h|_{x=0} = u_y^h|_{x=y=0} = 0$ constrained,
- $\mathbf{u}_2^h \sim$ complete bicubic polynomial expansion with $u_x^h|_{x=0} = u_y^h|_{x=y=0} = 0$ constrained.

The problem domain is partitioned into four equal-sized integration subdomains as shown in Fig. 2. DIE has been secured by a sufficiently high-order quadrature. Different quadratures are employed to compute the work done over the two boundary segments $-1 \leq y \leq 0$ and $0 \leq y \leq 1$ at $x = 10$. For problem 3, the orders of $\mathbf{N}^T \mathbf{n} \tilde{\boldsymbol{\sigma}}$'s at $x = 10$ for \mathbf{u}_1^h and \mathbf{u}_2^h are, respectively, second and third. Hence, the second-order quadrature is the minimal quadrature for BIE. For problem 4, the orders of $\mathbf{N}^T \mathbf{n} \tilde{\boldsymbol{\sigma}}$'s at $x = 10$ for \mathbf{u}_1^h and \mathbf{u}_2^h are, respectively, third and fourth. Hence, the second and third-order quadratures are, respectively, the minimal quadratures for BIE. Tables 3 and 4 list the displacement at A and the bending stress at B, see Fig. 2. Whenever the employed quadrature orders are lower than the minimal, it can be seen that the predictions are erroneous. The importance of BIE in securing linear and quadratic exactness is demonstrated.

Table 4
Predictions for problem 4 by using different quadratures to evaluate the work done

Trial solution	Minimum quadrature order for BIE	Employed quadrature order	$u_x^h _{x=10,y=0}$	$u_y^h _{x=10,y=0}$	$\left. \frac{du_x^h}{dx} \right _{x=5,y=1}$
u_1^h	2	1	Exact	-37.5000	0.7500
		2	Exact	Exact	Exact
		3	Exact	Exact	Exact
u_2^h	3	1	Exact	-37.4059	0.7474
		2	Exact	-49.9940	0.9998
		3	Exact	Exact	Exact

Commonly used mesh-free approximants such as those constructed by moving least-squares and reproducing kernel particle methods [2,3] contain non-polynomial components. Therefore, BIE and DIE cannot be secured by quadratures or, to be more specific, Gaussian quadratures even for linear exactness as illustrated in Ref. [13]. Nevertheless, the corresponding error decreases when the quadrature order and/or the number of integration subdomains increases.

3. Direct and stabilized nodal integrations

An efficient way to evaluate the weak form for Galerkin mesh-free methods is nodal integration whose core idea is to use nodes as the integration sampling points and sizes of the nodal subdomains as the weight factors. To this end, (7) is revised as

$$\Pi^* = \sum_{I=1} \mathbf{q}^T \left[\frac{A^I}{2} (\mathbf{LN})_I^T \mathbf{C} (\mathbf{LN})_I \mathbf{q} - \langle \mathbf{N}^T \bar{\mathbf{b}} \rangle_{\Omega_I} - \langle \mathbf{N}^T \bar{\mathbf{t}} \rangle_{\Gamma_I^I}^\# \right] \tag{12}$$

in which I is the nodal index, $(\)_I$ denotes the nodal value of the embraced term, A^I denotes the nodal subdomain size and the superscript # designates that the integral is computed for prescribing the boundary traction $\bar{\mathbf{t}}$. An efficient way to construct nodal subdomains is the Dirichlet tessellation which leads to the Voronoi cells [10].

In nodal integrations, the number of integration subdomains has been fixed by the number of nodes. Using the single-point quadrature which can secure the linear exactness only for linear trial solutions, the integration error for the trial solutions commonly employed in mesh-free methods appears to be significant. Though the system matrix arising from the above direct nodal integration is non-singular, its solutions are sometimes plagued by spurious oscillations which can be illustrated by the two one-dimensional problems in Example 2.1. The five-node Lagrangian interpolation is adopted as the trial solution. Oscillations of the results predicted by the direct nodal integration can be seen in Figs. 3 and 4. The predictions of the stabilized conforming (SC) nodal integration will be discussed in the next section. Beissel and Belytschko [11] stabilized the oscillation by penalizing Π^* with the square of the equilibrium

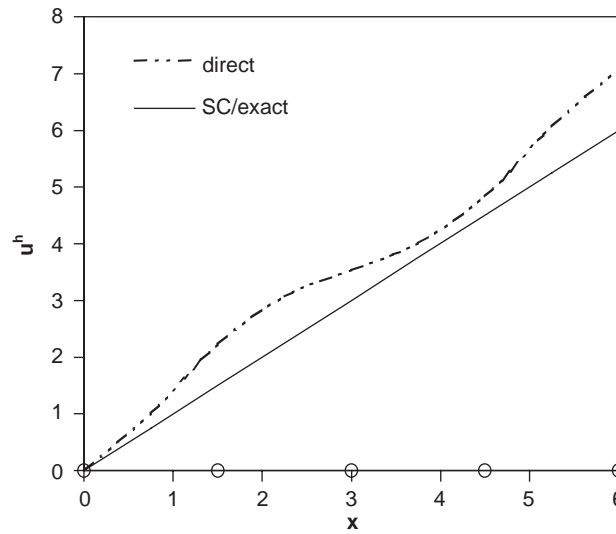


Fig. 3. Predictions for the zero body force problem. The trial solution is the five-node interpolation function and O's along x -axis denote nodal locations.

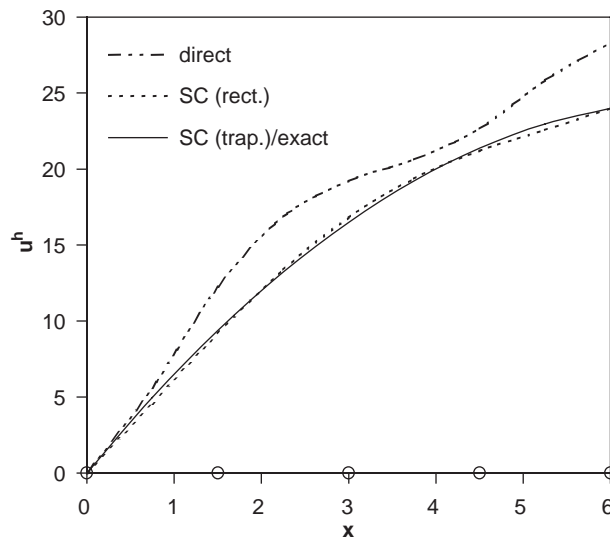


Fig. 4. Predictions for the constant body force problem. The trial solution is the five-node interpolation function and O's along x -axis denote nodal locations.

residue and led to

$$\begin{aligned} \Pi^{**} = \sum_{I=1} \left[\mathbf{q}^T \frac{A^I}{2} (\mathbf{LN})_I^T \mathbf{C} (\mathbf{LN})_I \mathbf{q} - \mathbf{q}^T A_I (\mathbf{N}^T \bar{\mathbf{b}})_I - \mathbf{q}^T \langle \mathbf{N}^T \bar{\mathbf{t}} \rangle_{\Gamma_I}^\# \right. \\ \left. + \alpha A^I (\mathbf{L}^T \mathbf{C} (\mathbf{LN})_I \mathbf{q} + \bar{\mathbf{b}})_I^T (\mathbf{L}^T \mathbf{C} (\mathbf{LN})_I \mathbf{q} + \bar{\mathbf{b}})_I \right]. \end{aligned} \tag{13}$$

The same stabilized nodal integration was later adopted by Bonet and Kulasegaram [12] who employed the smoothed particle hydrodynamics approximation. Nevertheless, the equilibrium residue involves the second-order derivatives which are costly and inaccurate to be computed. For problems that do not originally exhibit the spurious modes, the stabilization term can deteriorate the solution accuracy and the penalty factor must be chosen with care [13].

4. Stabilized conforming nodal integration

By considering the equilibrium of the prescribed boundary traction and the traction derived from the domain stress/strain, Chen and his coworkers [13–15] identified the integration constraint (IC) as the criteria for the Galerkin method to fulfill the linear consistency. The consistency is indeed the analogy of the satisfaction of the constant stress patch test in the finite element method. IC can be stated as

$$\langle \mathbf{LN}_I \rangle_\Omega = \langle \mathbf{n}^T \mathbf{N}_I \rangle_{\Gamma_I}^\# \quad (14)$$

where \mathbf{N}_I denotes the shape function matrix of the I th node. Obviously, $\langle \mathbf{LN}_I \rangle_\Omega$ vanishes when the support of the I th node does not overlap with Γ_I . Unlike (12) which uses the nodal gradient to evaluate the weak form, Chen and his coworkers employed the following smoothed nodal gradient in the stabilized conforming (SC) nodal integration [13–15]:

$$(\mathbf{LN})_I \simeq \frac{1}{A^I} \int_{\Omega^I} \mathbf{LN} \, d\Omega = \frac{1}{A^I} \int_{\partial\Omega^I} \mathbf{n}^T \mathbf{N} \, d\Gamma \simeq \frac{1}{A^I} \langle \mathbf{n}^T \mathbf{N} \rangle_{\partial\Omega^I}. \quad (15)$$

The second approximation “ \simeq ” arises from the numerical integration. Thus, (12) becomes:

$$\Pi^\circledast = \mathbf{q}^T \sum_{I=1} \left[\frac{1}{2A^I} \langle \mathbf{n}^T \mathbf{N} \rangle_{\partial\Omega^I}^T \mathbf{C} \langle \mathbf{n}^T \mathbf{N} \rangle_{\partial\Omega^I} \mathbf{q} - \langle \mathbf{N}^T \bar{\mathbf{b}} \rangle_{\Omega^I} - \langle \mathbf{N}^T \bar{\mathbf{t}} \rangle_{\Gamma_I^I}^\# \right] \quad (16)$$

and

$$\begin{aligned} \delta\Pi^\circledast = & \delta\mathbf{q}^T \sum_I \left[\frac{1}{A^I} \langle \mathbf{n}^T \mathbf{N} \rangle_{\Gamma_I^I}^T \mathbf{C} \langle \mathbf{n}^T \mathbf{N} \rangle_{\partial\Omega^I} \mathbf{q} - \langle \mathbf{N}^T \bar{\mathbf{b}} \rangle_{\Omega^I} - \langle \mathbf{N}^T \bar{\mathbf{t}} \rangle_{\Gamma_I^I}^\# \right] \\ & + \delta\mathbf{q}^T \sum_m \left[\frac{1}{A^{m+}} \langle \mathbf{N}^T \mathbf{n} \rangle_{\Gamma_m^+}^{m+} \mathbf{C} \langle \mathbf{n}^T \mathbf{N} \rangle_{\partial\Omega^{m+}} + \frac{1}{A^{m-}} \langle \mathbf{N}^T \mathbf{n} \rangle_{\Gamma_m^-}^{m-} \mathbf{C} \langle \mathbf{n}^T \mathbf{N} \rangle_{\partial\Omega^{m-}} \right] \mathbf{q}. \end{aligned} \quad (17)$$

To examine the requirements for linear exactness, \mathbf{q} , $\bar{\mathbf{b}}$ and $\bar{\mathbf{t}}$ are prescribed, respectively, to $\tilde{\mathbf{q}}$, $\mathbf{0}$ and $\mathbf{n}\tilde{\sigma}$ such that $\tilde{\mathbf{u}} = \mathbf{N}\tilde{\mathbf{q}}$ is an arbitrary linear displacement field and $\tilde{\sigma} = \mathbf{C}(\mathbf{LN})\tilde{\mathbf{q}}$ is the corresponding constant stress field. Assuming

$$\tilde{\sigma} = \frac{1}{A^I} \mathbf{C} \langle \mathbf{n}^T \mathbf{N} \rangle_{\partial\Omega^I} \tilde{\mathbf{q}} = \frac{1}{A^I} \mathbf{C} \langle \mathbf{n}^T \tilde{\mathbf{u}} \rangle_{\partial\Omega^I} \quad (18)$$

then

$$\delta\Pi^\circledast|_{\mathbf{q}=\tilde{\mathbf{q}}, \bar{\mathbf{b}}=\mathbf{0}, \bar{\mathbf{t}}=\mathbf{n}\tilde{\sigma}} = \delta\mathbf{q}^T \sum_I [\langle \mathbf{N}^T \mathbf{n} \rangle_{\Gamma_I^I} - \langle \mathbf{N}^T \mathbf{n} \rangle_{\Gamma_I^I}^\#] \tilde{\sigma} + \delta\mathbf{q}^T \sum_m [\langle \mathbf{N}^T \mathbf{n} \rangle_{\Gamma_m^+}^{m+} + \langle \mathbf{N}^T \mathbf{n} \rangle_{\Gamma_m^-}^{m-}] \tilde{\sigma}. \quad (19)$$



Fig. 5. O's are nodes and +'s are node-to-node midpoints. O's and +'s are the sampling points of the body forces in SC nodal (rect.) and SC nodal (trap.), respectively.

Should the system matrix be non-singular, the sufficient conditions for $\mathbf{q} = \tilde{\mathbf{q}}$, $\bar{\mathbf{b}} = \mathbf{0}$ and $\bar{\mathbf{t}} = \mathbf{n}\tilde{\sigma}$ being the unique solution of the above weak form are the following boundary integration consistency (BIC) requirements:

$$\langle \mathbf{N}^T \mathbf{n} \rangle_{\Gamma^I} = \langle \mathbf{N}^T \mathbf{n} \rangle_{\Gamma^I}^* + \langle \mathbf{N}^T \mathbf{n} \rangle_{\Gamma_m}^{m+} + \langle \mathbf{N}^T \mathbf{n} \rangle_{\Gamma_m}^{m-} = 0. \tag{20}$$

If non-polynomial terms are involved in the trial solution, it will not be possible to evaluate $\langle \mathbf{N}^T \mathbf{n} \rangle$ exactly by mid-point, trapezoidal or Gaussian rules. Fortunately, when the same integration rule is applied to evaluate the two integrands in the first BIC requirement and the two integrands in the second BIC requirement, pairwise cancellation of traction similar to that of the free formulation [16–18] will occur.

Unlike BIE, exactness is not posed by BIC. BIC is far less demanding and can easily be satisfied, for instances, by using the same integration rule to evaluate all integrands over the same boundary segment. The practice is not only natural but also the one employed in SC nodal integration [13–15]. This completes the proof for the linear exactness of the SC nodal integration. By merging and assembling the two BIC requirements, one can obtain:

$$\langle \mathbf{N}^T \mathbf{n} \rangle_{\partial\Omega} = \langle \mathbf{N}^T \mathbf{n} \rangle_{\Gamma_t}^* \tag{21}$$

which is equivalent to the IC in (14) posed for linear exactness in Ref. [13]. Hence, this paragraph presents not only an explicit proof but also a more “microscopic” analysis for SC nodal integration.

The two problems in Example 2.1 are repeated by using the five-node interpolation and SC nodal integration. Linear exactness is yielded as shown in Fig. 3. To compute the system matrix of one-dimensional problems, SC nodal integration only needs to compute the trial solution at the node-to-node mid-points and the two boundary nodes, see Fig. 5. Hence, it is more efficient to account for the body force by using the trapezoidal rule than the rectangular rule. The two practices lead to respectively SC(trap.) and SC(rect.) in Fig. 4. The former yields quadratic exactness in this illustration, which employs a polynomial trial solution, and the latter is less accurate.

5. Variational basis of SC nodal integration

Strain smoothing in SC nodal integration was introduced into the Galerkin mesh-free methods through the assumed strain method [13]. In this section, the basis of SC nodal integration and thus the strain smoothing will be provided by a classical variational functional for domain decomposition. By taking stress and displacement as the independent field variables as well as treating e.b.c. and displacement compatibility as prerequisites, the strong form of the problem can be summarized as

$$\text{stress–displacement relation: } \boldsymbol{\sigma} = \mathbf{C}(\mathbf{L}\mathbf{u}) \quad \text{in all } \Omega^I\text{'s,} \tag{22}$$

$$\text{stress equilibrium condition: } \mathbf{L}^T \boldsymbol{\sigma} + \bar{\mathbf{b}} = \mathbf{0} \quad \text{in all } \Omega^I\text{'s,} \tag{23}$$

$$\text{traction reciprocity: } (\mathbf{n}\boldsymbol{\sigma})^{m+} + (\mathbf{n}\boldsymbol{\sigma})^{m-} = \mathbf{0} \quad \text{on all } \Gamma'_m \text{ s,} \quad (24)$$

$$\text{n.b.c.: } \mathbf{n}\boldsymbol{\sigma} = \bar{\mathbf{t}} \quad \text{on all } \Gamma'_i. \quad (25)$$

The following is the domain-decomposed version of the well-known Hellinger–Reissner functional [18–21]:

$$\Pi_{\text{HR}} = \sum_I \left(\int_{\Omega^I} \left[-\frac{1}{2} \boldsymbol{\sigma}^T \mathbf{C}^{-1} \boldsymbol{\sigma} + \boldsymbol{\sigma}^T (\mathbf{L}\mathbf{u}) - \mathbf{u}^T \bar{\mathbf{b}} \right] d\Omega - \int_{\Gamma'_i} \mathbf{u}^T \bar{\mathbf{t}} d\Gamma \right). \quad (26)$$

By virtue of the divergence theorem,

$$\begin{aligned} \delta \Pi_{\text{HR}} = & \sum_I \left(\int_{\Omega^I} [\delta \boldsymbol{\sigma}^T (-\mathbf{C}^{-1} \boldsymbol{\sigma} + \mathbf{L}\mathbf{u}) - (\mathbf{L}^T \boldsymbol{\sigma} + \bar{\mathbf{b}})^T \delta \mathbf{u}] d\Omega + \int_{\Gamma'_i} \delta \mathbf{u}^T (\mathbf{n}\boldsymbol{\sigma} - \bar{\mathbf{t}}) d\Gamma \right) \\ & + \sum_m \int_{\Gamma_m} \delta \mathbf{u}^T [(\mathbf{n}\boldsymbol{\sigma})^{m+} + (\mathbf{n}\boldsymbol{\sigma})^{m-}] d\Gamma, \end{aligned} \quad (27)$$

it can be seen that (22)–(25) are enforced by the stationary nature of Π_{HR} . For $\boldsymbol{\sigma}$ satisfying the homogeneous equilibrium condition, i.e. $\mathbf{L}^T \boldsymbol{\sigma} = \mathbf{0}$,

$$\Pi_{\text{HR}} = \sum_I \left(\int_{\Omega^I} \left[-\frac{1}{2} \boldsymbol{\sigma}^T \mathbf{C}^{-1} \boldsymbol{\sigma} - \mathbf{u}^T \bar{\mathbf{b}} \right] d\Omega + \int_{\partial\Omega^I} (\mathbf{n}\boldsymbol{\sigma})^T \mathbf{u} d\Gamma - \int_{\Gamma'_i} \mathbf{u}^T \bar{\mathbf{t}} d\Gamma \right). \quad (28)$$

In hybrid element formulation, the use of homogeneous equilibrating stress enables the element stiffness matrix to be constructed by defining the displacement along the element boundary only. This is particularly advantageous when a compatible displacement cannot be constructed inside the element subdomain [19–21]. With the homogeneous equilibrating trial stress expressed as

$$\boldsymbol{\sigma} = \mathbf{P}\boldsymbol{\beta}^I \quad (29)$$

in which \mathbf{P} is the stress shape function matrix and $\boldsymbol{\beta}^I$ is the vector of coefficients for the I th nodal subdomain, (28) becomes

$$\begin{aligned} \Pi_{\text{HR}} = & \sum_I \left(-\frac{1}{2} (\boldsymbol{\beta}^I)^T \int_{\Omega^I} \mathbf{P}^T \mathbf{C}^{-1} \mathbf{P} d\Omega \cdot \boldsymbol{\beta}^I + (\boldsymbol{\beta}^I)^T \int_{\partial\Omega^I} \mathbf{P}^T \mathbf{n}^T \mathbf{N} d\Gamma \cdot \mathbf{q} - \mathbf{q}^T \right. \\ & \left. \times \int_{\Omega^I} \mathbf{N}^T \bar{\mathbf{b}} d\Omega - \mathbf{q}^T \int_{\Gamma'_i} \mathbf{N}^T \bar{\mathbf{t}} d\Gamma \right). \end{aligned} \quad (30)$$

The stationary nature of the functional with respect to $\boldsymbol{\beta}^I$'s gives

$$\int_{\Omega^I} \mathbf{P}^T \mathbf{C}^{-1} \mathbf{P} d\Omega \cdot \boldsymbol{\beta}^I = \int_{\partial\Omega^I} \mathbf{P}^T \mathbf{n}^T \mathbf{N} d\Gamma \cdot \mathbf{q} \quad (31)$$

with which

$$\begin{aligned} \Pi_{HR} = \mathbf{q}^T \sum_I \left(\frac{1}{2} \left(\int_{\partial\Omega^I} \mathbf{P}^T \mathbf{n}^T \mathbf{N} \, d\Gamma \right)^T \left(\int_{\Omega^I} \mathbf{P}^T \mathbf{C}^{-1} \mathbf{P} \, d\Omega \right)^{-1} \left(\int_{\partial\Omega^I} \mathbf{P}^T \mathbf{n}^T \mathbf{N} \, d\Gamma \right) \mathbf{q} \right. \\ \left. - \int_{\Omega^I} \mathbf{N}^T \bar{\mathbf{b}} \, d\Omega - \int_{\Gamma_t^I} \mathbf{N}^T \bar{\mathbf{t}} \, d\Gamma \right). \end{aligned} \tag{32}$$

When \mathbf{P} is chosen to be the identity matrix and numerical integration is invoked, the functional will be

$$\Pi_{HR}^\# = \mathbf{q}^T \sum_{I=1} \left[\frac{1}{2A^I} \langle \mathbf{n}^T \mathbf{N} \rangle_{\partial\Omega^I}^T \mathbf{C} \langle \mathbf{n}^T \mathbf{N} \rangle_{\partial\Omega^I} \mathbf{q} - \langle \mathbf{N}^T \bar{\mathbf{b}} \rangle_{\Omega^I} - \langle \mathbf{N}^T \bar{\mathbf{t}} \rangle_{\Gamma_t^I}^* \right] \tag{33}$$

which is identical to Π^\circledast in (16). In this light, the SC nodal integration is justified variationally by the classical Hellinger–Reissner Principle.

6. Numerical examples

As a large number of one- and two-dimensional linear and nonlinear problems have been studied by SC nodal integration using the reproducing kernel particle approximants [13–15], only a few examples will be shown here to contrast the direct and stabilized conforming nodal integrations. Moreover, the moving least-squares (MLS) approximants [2] will be employed. For completeness, a brief introduction to the MLS method is presented in Appendix A. The weight function is taken to be the C^2 quartic spline function. To facilitate the subsequent discussion, the following abbreviations are defined:

- N_n —the number of uniformly distributed nodes in the problem;
- N_p —the order of the MLS basis functions (1 for linear basis, 2 for quadratic basis);
- L_n —nodal spacing;
- R —support radius of the weight function.

Example 6.1. *1D problem with zero body force, see Example 2.1:* Problem 1 is repeated with $N_n = 7$, $N_p = 2$ and $R = 3L_n$. It can be seen in Fig. 6 that SC nodal integration yields the exact solution whereas direct nodal integration deviates slightly from the exact solution. Oscillation of results predicted by direct nodal integration can be seen but is not obvious.

Example 6.2. *1D problem with constant body force, see Example 2.1:* Problem 2 is repeated with $N_n = 7$, $N_p = 2$ and $R = 3L_n$. Slight oscillation of results predicted by direct nodal integration can be noted in Fig. 7. For both kinds of nodal integrations, the use of the trapezoidal rule to account for the body force yields more accurate results than the use of the rectangular rule. Though SC(trap) graphically overlaps the exact solution, they differ numerically. In other words, the present SC(trap) does not attain quadratic exactness as the one that employs purely polynomial terms in the trial solutions, see Fig. 4.

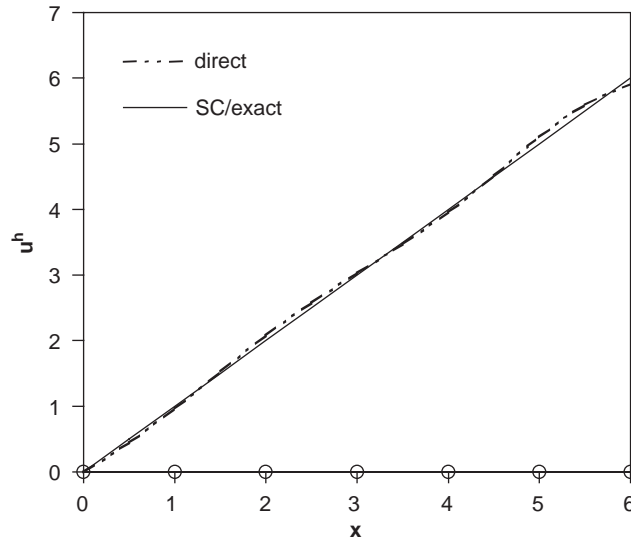


Fig. 6. Predictions for the zero body force problem. The trial solution is obtained by MLS with $N_n = 7$, $N_p = 2$ and $R = 3L_n$. O's along the x -axis denote nodal locations.

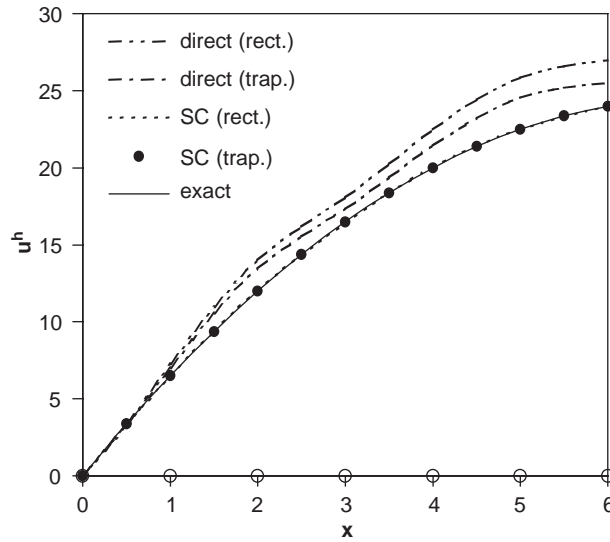


Fig. 7. Predictions for the constant body force problem. The trial solution is obtained by MLS with $N_n = 7$, $N_p = 2$ and $R = 3L_n$. O's along the x -axis denote nodal locations.

Example 6.3. *1D problem with linear body force:* The following problem was considered by Beissel and Belystchko [11] and is excellent for demonstrating the spurious oscillation:

$$\frac{d^2u}{dx^2} + \frac{x}{10} = 0 \quad \text{for } 0 \leq x \leq 10, \quad u|_{x=0} = u|_{x=10} = 0 \Rightarrow u = \frac{5x}{3} \left(1 - \frac{x^2}{100} \right).$$

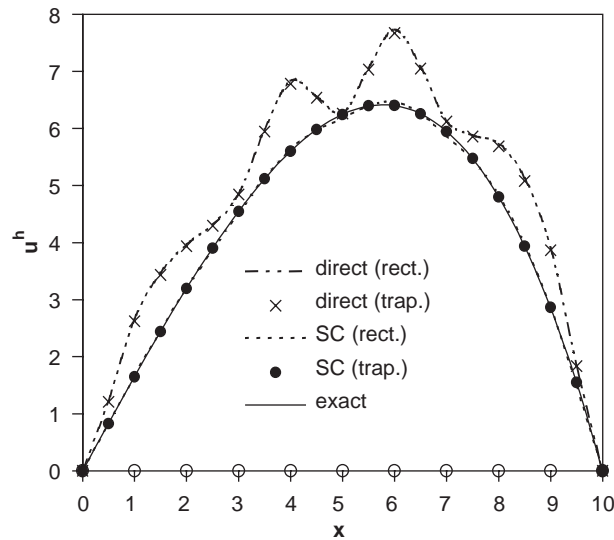


Fig. 8. Effect of rectangular and trapezoidal rules in accounting for linear body force. The trial solution is obtained by MLS with $N_n = 11$, $N_p = 2$ and $R = 3L_n$. O's along the x -axis denote nodal locations.

By using $N_n = 11$, $R = 3L_n$ and $N_p = 2$, Fig. 8 shows again that the use of the trapezoidal rule to account for the body force yields marginally more accurate results than the use of the rectangular rule in accounting for the body force. It can be seen that SC(trap.) graphically overlaps with the exact solution. Spurious oscillation is obvious in the predictions of direct nodal integration. Since the rectangular and trapezoidal rules are most natural to evaluate the body force term in, respectively, the direct and the SC nodal integrations, they will be adopted accordingly in the remaining studies. Figs. 9 and 10 examine the predictions of direct nodal integration by using different R , N_p and N_n . It is worthwhile to note that the results actually diverge from the exact solution as the number of nodes increase. On the other hand, the use of higher N_n in SC nodal integration yields progressively more accurate results as seen in Figs. 11 and 12.

Regarding the source of the strong spurious oscillation in the direct nodal integration, it is interesting to note that both the nodal gradient (used in direct nodal integration) and the smoothed nodal gradient (used in SC nodal integration) are independent of the nodal parameters at the same node (for the node whose support does not reach the boundary). Hence, this independence does not appear to be the cause of the oscillation. A more convincing cause is probably the poor enforcement of the traction reciprocity in the direct nodal integration.

Example 6.4. *A simply-supported beam subjected to mid-span force:* For a thin beam with its centroidal axis bounded by $x \in [x_S, x_T]$ and coincident with the x -axis, the inplane strain is $\epsilon_{xx} = -zw_{,xx}$ and the strain energy is

$$U = \frac{1}{2} \int_{x_S}^{x_T} \int_{-h/2}^{+h/2} E \epsilon_{xx}^2 dz dx = \frac{1}{2} \int_{x_S}^{x_T} \int_{-h/2}^{+h/2} z^2 E w_{,xx}^2 dz dx = \frac{1}{2} \int_{x_S}^{x_T} E^b w_{,xx}^2 dx$$

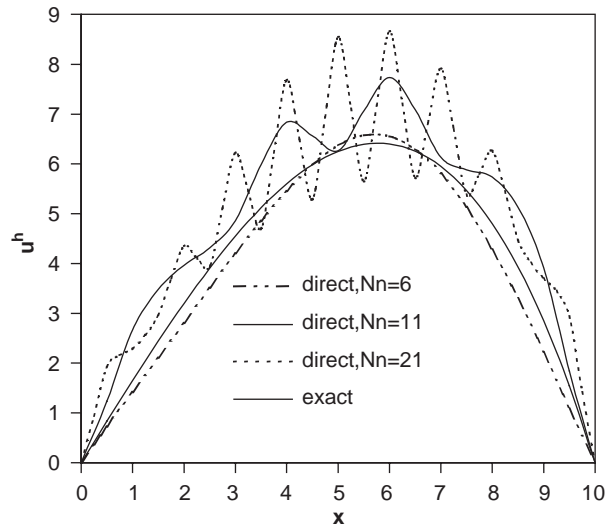


Fig. 9. Predictions of direct nodal integration for the linear body force problem. The trial solutions are obtained by MLS with $N_p = 2$ and $R = 3L_n$.

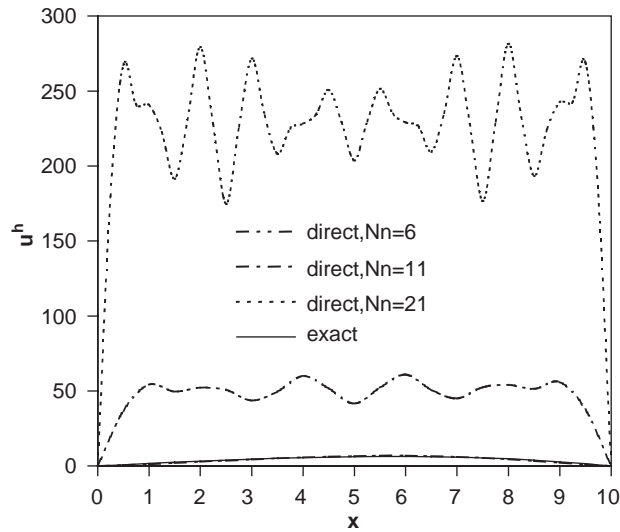


Fig. 10. Predictions of direct nodal integration for the linear body force problem. The trial solutions are obtained by MLS with $N_p = 3$ and $R = 4L_n$.

where

$$h \text{ is the beam thickness and } E^b = \int_{-h/2}^{+h/2} z^2 E \, dx.$$

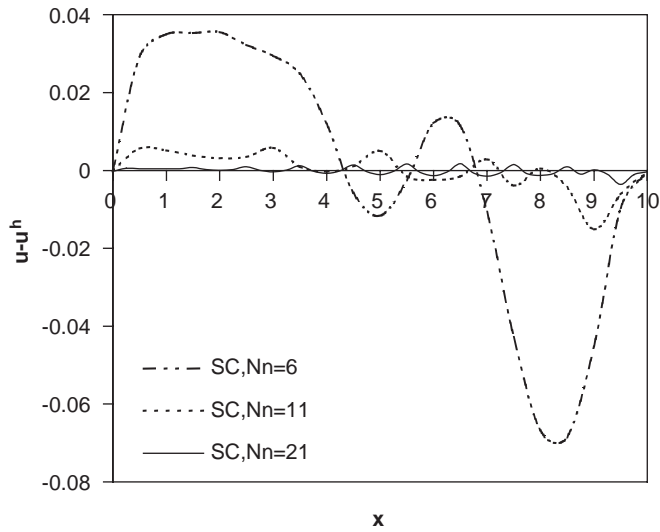


Fig. 11. Errors of SC nodal integration for the linear body force problem. The trial solutions are obtained by MLS with $N_p = 2$ and $R = 3L_n$.

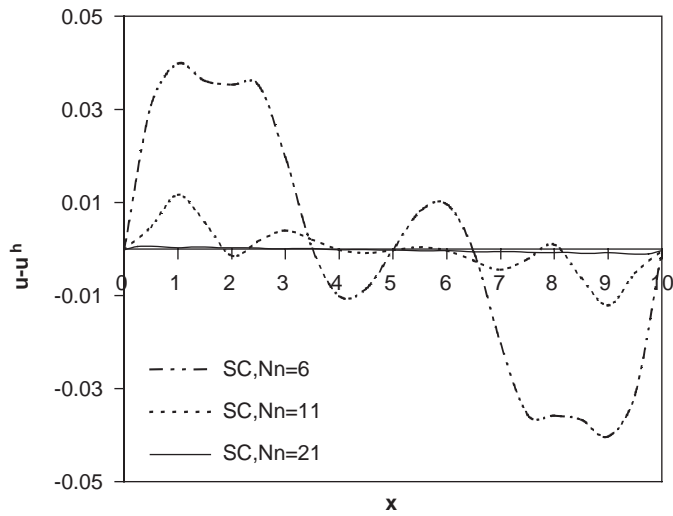


Fig. 12. Errors of SC nodal integration for the linear body force problem. The trial solutions are obtained by MLS with $N_p = 3$ and $R = 4L_n$.

Using the SC nodal integration, the strain energy in a nodal subdomain $x \in [x_S^I, x_T^I]$ becomes

$$U^I = \frac{E^b}{2} (\bar{w}_{,xx}^I)^2$$

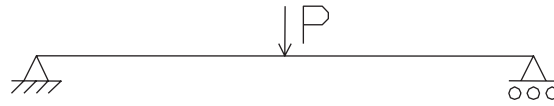


Fig. 13. A simply-supported beam loaded at its mid-span.

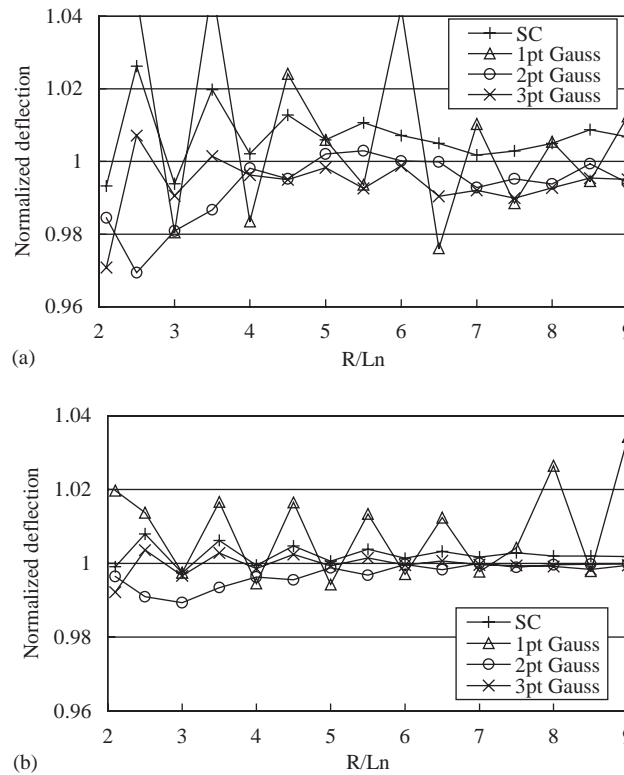


Fig. 14. Normalized deflection under P for see Fig. 13: (a) $N_p = 2$ and $N_n = 11$; (b) $N_p = 2$ and $N_n = 21$.

where

$$\bar{w}_{,xx}^I = \int_{x_S^I}^{x_T^I} w_{,xx} \, dx = (w_{,x})|_{x=x_T^I} - (w_{,x})|_{x=x_S^I}.$$

Fig. 13 shows a simply-supported beam with a mid-span force P acting. The thin-beam solution for the mid-span deflection is $(Pl^3)/(4Eh^3)$ where l is the beam length and h is the beam thickness. After normalized by the thin-beam solution, the predicted mid-span deflections are plotted against R/L_n in Fig. 14 for quadratic basis (i.e. $N_p = 2$). The results of the SC nodal integration and the ones obtained by domain integration of the strain energy with the one-, two- and three-point quadratures in each node-to-node subdomain are shown. The results of the SC nodal integration are more accurate than, close to and less accurate than that of the one-, two- and three-point quadratures, respectively. However, the SC nodal integration is more economic than all the quadrature scheme due to the reduction of derivative order.

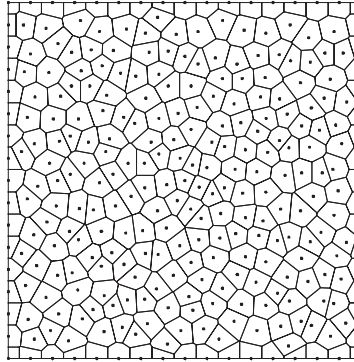


Fig. 15. The Voronoi cells for a simply-supported square plate modeled by 17×17 non-uniformly distributed nodes.

Example 6.5. *A thin square plate subjected to central point force:* For a plate with its mid-plane A at $z=0$, the vector of inplane strain components is: $\epsilon = z\epsilon^b$ where $\epsilon^b = -\{w_{,xx}, w_{,yy}, 2w_{,xy}\}^T$ is the vector of bending strain components. The strain energy is:

$$U = \frac{1}{2} \int_A \int_{-h/2}^{+h/2} z^2 (\epsilon^b)^T \mathbf{C} (\epsilon^b) dz dA = \frac{1}{2} \int_A (\bar{\epsilon}^b)^T \mathbf{C}^b \bar{\epsilon}^b dA$$

where \mathbf{C} is the elasticity matrix with the plane stress condition incorporated along the z -direction and

$$\mathbf{C}^b = \int_{-h/2}^{+h/2} z^2 \mathbf{C} dz.$$

Using the SC nodal integration, the strain energy in the nodal subdomain A^I is

$$U^I = \frac{A^I}{2} (\bar{\epsilon}^{bI})^T \mathbf{C}^b (\bar{\epsilon}^{bI})$$

where

$$\begin{aligned} \bar{\epsilon}^{bI} &= \int_A \epsilon^b dA = - \int_A \{w_{,xx}, w_{,yy}, 2w_{,xy}\}^T dA \\ &= - \oint_{\partial A} \{n_x w_{,x}, n_y w_{,y}, n_x w_{,y} + n_y w_{,x}\} ds \end{aligned}$$

and $\{n_x, n_y\}^T$ is the unit normal to ∂A , namely, the boundary of A .

A simply-supported square plate of side length a subjected to a central point load P is considered. The converged Navier solution for the central deflection is: $0.0116 Pa^2/D$ where D is the flexural rigidity of the plate. Again, the quadratic basis is used in MLS approximation. The plate is modeled by 11×11 uniformly, 17×17 uniformly, and 17×17 non-uniformly distributed nodes. The Voronoi cells for the 17×17 non-uniformly distributed nodes are shown in Fig. 15. Fig. 16 shows the normalized central deflections predicted by the SC nodal integration and by applying the third order Gaussian rule to the square subdomains with the uniformly distributed nodes being their corners. Despite of the shape

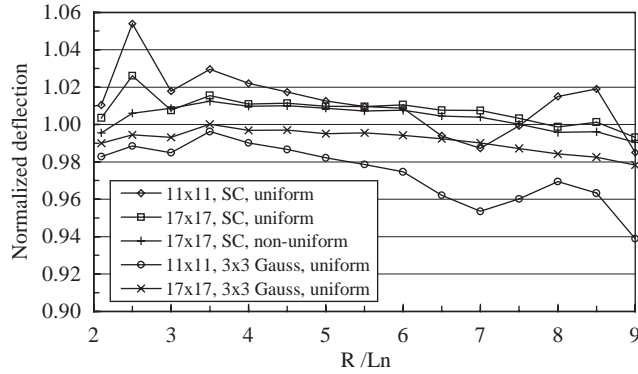


Fig. 16. Normalized central deflection for a simply-supported square plate subjected to a central point load, quadratic basis is employed.

contrast in the computational effort, it can be seen that the two integration schemes yield close accuracy. The predictions of the SC nodal integration in the 17×17 uniformly and non-uniformly distributed nodes are very close. This is probably due to the inherent insensitivity of the MLS toward nodal uniformity. The predictions of the first- and second-order Gaussian rules are also computed but they are all worse than that of the third-order Gaussian rule.

Example 6.6. *A thin circular arc subjected to mid-span force:* A brief account on computing the physical membrane and bending strains for thin shells with position vector $\mathbf{x} = \mathbf{x}_o(\xi, \eta) + \zeta \mathbf{x}_n(\xi, \eta)$ and displacement vector $\mathbf{u} = \mathbf{u}_o(\xi, \eta) + \zeta \mathbf{u}_n(\xi, \eta)$ where ξ and η are parametric coordinates and ζ is the transverse coordinate along the director \mathbf{u}_n can be found in Appendix B. For a circular arc with mean radius R , $\xi = \theta \in [\theta_S, \theta_T]$, $\eta = z$, $\mathbf{u}_o = \{u, v, 0\}^T$ and $\mathbf{x}_o = \{R \cos \theta, R \sin \theta, 0\}^T$. With $\mathbf{e}_1 = \{-\sin \theta, \cos \theta, 0\}^T$ which is tangential to $\mathbf{x}_{o,\theta}$, the membrane and bending strains can be derived to be

$$\varepsilon^m = \varepsilon_{11}^m = \frac{1}{R}(-u_{,\theta} \sin \theta + v_{,\theta} \cos \theta), \quad \varepsilon^b = \varepsilon_{11}^b = \frac{1}{R^2} \varepsilon_{\theta\theta}^b = \frac{-1}{R^2}(u_{,\theta\theta} \cos \theta + v_{,\theta\theta} \sin \theta)$$

and strain energy is

$$U = \frac{R}{2} \int_{\theta_S}^{\theta_T} \int_{-h/2}^{+h/2} E[(\varepsilon_{11}^m)^2 + \zeta(\varepsilon_{11}^b)^2] d\zeta d\theta = \frac{R}{2} \int_{\theta_S}^{\theta_T} [E^m(\varepsilon_{11}^m)^2 + E^b(\varepsilon_{11}^b)^2] d\theta$$

where

$$E \text{ is the elastic modulus, } E^m = \int_{-h/2}^{+h/2} E d\zeta \quad \text{and} \quad E^b = \int_{-h/2}^{+h/2} \zeta^2 E d\zeta.$$

Using the notion of the SC nodal integration to smooth the displacement derivatives, the strain energy for the nodal subdomain defined at $\theta = \theta^I$ and bounded by θ_S^I and θ_T^I is

$$U^I = \frac{R}{2} [E^m(\bar{\varepsilon}^{mI})^2 + E^b(\bar{\varepsilon}^{bI})^2]$$

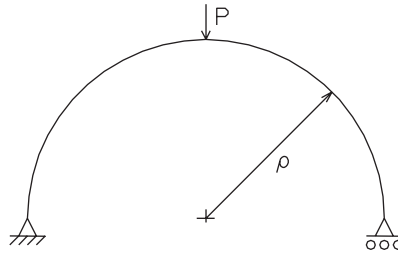


Fig. 17. A simply-supported arc loaded at its mid-span.

where

$$\bar{\varepsilon}^{mI} = -\frac{1}{R}(u|_{\theta=\theta_T^I} - u|_{\theta=\theta_S^I}) \sin \theta^I + \frac{1}{R}(v|_{\theta=\theta_T^I} - v|_{\theta=\theta_S^I}) \cos \theta^I,$$

$$\bar{\varepsilon}^{bI} = -\frac{1}{R^2}[(u,_{\theta}|_{\theta=\theta_T^I} - u|_{\theta=\theta_S^I}) \cos \theta^I + (v,_{\theta}|_{\theta=\theta_T^I} - v|_{\theta=\theta_S^I}) \sin \theta^I].$$

Fig. 17 shows a simply-supported semi-circular arc subjected to a mid-span force P . The analytical thin-arc solution, which accounts for the bending and membrane deformation, for the deflection of the point under P is derived to be

$$\frac{P}{E} \frac{\rho}{h} \left[\frac{\pi}{8} + \frac{3(3\pi - 8)}{2} \left(\frac{\rho}{h}\right)^2 \right]$$

where ρ and h are, respectively, the mean radius and thickness of the arc. Same as the last two examples, only quadratic basis is employed in the MLS approximation. Figs. 18a and b show the normalized deflections for $\rho/h = 50$ by using 15 and 31 uniformly distributed nodes along the arc, respectively. The weak form is evaluated by the SC nodal integration as well as the domain integration with one-, two- and three-point quadratures in each node-to-node subdomain. It can be seen that all integration schemes yield more accurate results when more nodes are employed. Among them, the SC nodal integration is the most accurate whereas the results yielded by the one- and three-point quadratures are too “soft” and too “stiff”, respectively. By fixing the number of nodes to 31, Fig. 18c shows the normalized deflections for $\rho/h = 500$. By comparing Figs. 18b and c, it can be seen that the normalized results of the SC nodal integration and the one-point quadrature are un-affected by the aspect ratio ρ/h . On the other hand, the normalized results of the two- and three-point quadratures drop when ρ/h is increased. This is an indication that the membrane strain energy is excessively sampled. In this constrained problem (with zero membrane strain), the most accurate integration scheme is the SC nodal integration.

7. Closure

Galerkin mesh-free methods are examined from a domain decomposition perspective. Presuming the analytical solution is admissible in the trial solution, requirements on integration exactness are identified for the strict satisfaction of traction reciprocity and natural boundary condition in the weak form. Mesh-free approximants often contain non-polynomial terms. When they are employed in the trial solution,

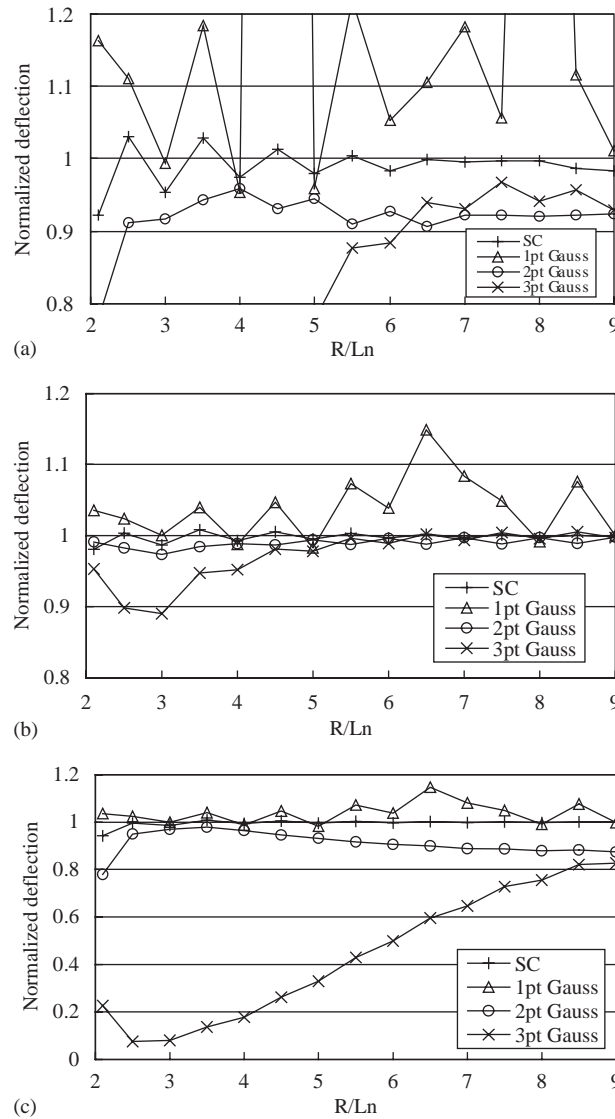


Fig. 18. Normalized deflections under the loading force in a simply-supported arc, see Fig. 17: (a) $N_p = 2, N_n = 15, \rho/h = 50$; (b) $N_p = 2, N_n = 31, \rho/h = 50$; (c) $N_p = 2, N_n = 31, \rho/h = 500$.

the corresponding weak form cannot be exactly integrated by Gaussian quadratures. Consequently, they fail to reproduce any order of exactness. Recently, stabilized conforming nodal integration for Galerkin mesh-free methods was proposed and illustrated to be linearly exact. Provided that the same numerical integration rule is applied to integrands over the same boundary segments, this paper presents a direct proof of the linear exactness of the integration. It also shows that the integration method can be formulated by the Hellinger–Reissner Principle and thus justified in light of the classical variational sense. Applications of the method to straight beam, plate and curved beam problems are presented. Overall speaking, the SC nodal integration offers the best combination of accuracy and computational efficiency.

Acknowledgements

The financial support of the University of Hong Kong in the form of a Small Project Funding Program is gratefully acknowledged.

Appendix A. Moving least-squares method

Trial solutions in the Galerkin mesh-free methods can be constructed by different methods. Among them, moving least square (MLS) and reproducing kernel particle approximations are probably the most popular ones [2,3]. Provided the same monomial basis is employed, both approximations will yield the same trial solution. In the MLS, an approximation $f(\mathbf{x})$ localized at \mathbf{x} is expressed as the following inner product:

$$f(\mathbf{x}) = \mathbf{p}^T(\mathbf{x}) \cdot \mathbf{a}(\mathbf{x}) \quad (\text{A.i})$$

where $\mathbf{p}(\mathbf{x})$ is a vector comprising a set of monomial basis functions and $\mathbf{a}(\mathbf{x})$ is the associated vector of coefficients. In two-dimensions, $\mathbf{p}^T(\mathbf{x}) = [1, x_1, x_2]$ and $\mathbf{p}^T(\mathbf{x}) = [1, x_1, x_2, x_1^2, x_1x_2, x_2^2]$ for the linear and quadratic bases, respectively. The coefficient vector is determined by minimizing the following term with respect to the coefficient vector:

$$J(\mathbf{x}) = \sum_{I=1}^N w_I(\mathbf{x}) (\mathbf{p}^T(\mathbf{x}_I) \cdot \mathbf{a}(\mathbf{x}) - f_I)^2 \quad (\text{A.ii})$$

in which \mathbf{x}_I , $w_I(\mathbf{x}) = w(\mathbf{x} - \mathbf{x}_I)$ and f_I are the coordinate vector, weight function and the datum of the I th node, respectively. Moreover, N is the number of nodes whose weight functions are non-zero at \mathbf{x} . The minimization yields:

$$\mathbf{a}(\mathbf{x}) = \mathbf{A}^{-1}(\mathbf{x}) \cdot \mathbf{D}(\mathbf{x}) \cdot \underline{\mathbf{f}} \quad (\text{A.iii})$$

where

$$\mathbf{A}(\mathbf{x}) = \sum_{I=1}^N w_I(\mathbf{x}) \cdot \mathbf{p}(\mathbf{x}_I) \cdot \mathbf{p}^T(\mathbf{x}_I), \quad \mathbf{D}(\mathbf{x}) = [w_1(\mathbf{x})\mathbf{p}(\mathbf{x}_1), \dots, w_N(\mathbf{x})\mathbf{p}(\mathbf{x}_N)],$$

$$\underline{\mathbf{f}} = [f_1, \dots, f_N]^T.$$

Back substitution of (A.iii) into (A.i) gives

$$f(\mathbf{x}) = \phi(\mathbf{x}) \cdot \underline{\mathbf{f}} \quad (\text{A.iv})$$

in which $\phi(\mathbf{x}) = \mathbf{p}^T(\mathbf{x}) \cdot \mathbf{A}^{-1}(\mathbf{x}) \cdot \mathbf{D}(\mathbf{x})$ is the shape function matrix. As the MLS is non-interpolatory,

$$f(\mathbf{x}_I) = \phi(\mathbf{x}_I) \cdot \underline{\mathbf{f}} \neq f_I \quad (\text{A.v})$$

in general. The first derivative of $f(\mathbf{x})$ with respect to x_i can be derived by chain rule:

$$f_{,i} = \phi_{,i} \underline{\mathbf{f}} = [\mathbf{p}_{,i}^T \mathbf{A}^{-1} \mathbf{D} + \mathbf{p}^T \mathbf{A}^{-1} (\mathbf{D}_{,i} - \mathbf{A}_{,i} \mathbf{A}^{-1} \mathbf{D})] \cdot \underline{\mathbf{f}}. \quad (\text{A.vi})$$

Similarly, higher order derivatives can be obtained. It can be seen that calculating derivatives and, especially, calculating higher order derivatives for MLS approximation is rather costly.

The continuity order of $f(\mathbf{x})$ is the same as the weight function $w(\mathbf{x})$. Commonly-used weight functions include exponential, Gaussian and spline functions which are at least C^1 . For instance, a widely-used spline is

$$w(r) = \begin{cases} 1 - 6(r/R)^2 + 8(r/R)^3 - 3(r/R)^4 & \text{for } r \leq 1 \\ 0 & \text{otherwise} \end{cases} \quad (\text{A.vii})$$

in which $r = \|\mathbf{x} - \mathbf{x}_I\|$ is the radial distance and R is the support radius. It can be checked that the function is C^2 .

Appendix B. Strains in thin shells

Let ξ and η be parametric coordinates of the mid-surface \mathbf{x}_o of the shell and $\zeta \in [-h/2, +h/2]$ be the physical transverse coordinate, the position and displacement vectors of the shell can be expressed as

$$\mathbf{x} = \mathbf{x}_o(\xi, \eta) + \zeta \mathbf{x}_n(\xi, \eta), \quad \mathbf{u} = \mathbf{u}_o(\xi, \eta) + \zeta \mathbf{u}_n(\xi, \eta)$$

where $\mathbf{x}_n = \mathbf{x}_{o,\xi} \times \mathbf{x}_{o,\eta} / j$ and $j = \|\mathbf{x}_{o,\xi} \times \mathbf{x}_{o,\eta}\|$. The linear covariant inplane strain ε_{ij} and transverse shear strain $\varepsilon_{\zeta i}$ are

$$\varepsilon_{ij} = (\mathbf{x}_{,i}^T \mathbf{u}_{,j} + \mathbf{x}_{,j}^T \mathbf{u}_{,i}) / 2 = \varepsilon_{ij}^m + \zeta \varepsilon_{ij}^b + \zeta^2\text{-terms}, \quad \varepsilon_{\zeta i} = (\mathbf{x}_{,\zeta}^T \mathbf{u}_{,i} + \mathbf{x}_{,i}^T \mathbf{u}_{,\zeta}) / 2 = \varepsilon_{\zeta i}^o + \zeta\text{-terms}$$

where

$$i, j = \xi \text{ and } \eta, \varepsilon_{\zeta i}^o = \mathbf{x}_n^T \mathbf{u}_{o,i} + \mathbf{x}_{o,i}^T \mathbf{u}_n, \quad \varepsilon_{ij}^m = (\mathbf{x}_{o,i}^T \mathbf{u}_{o,j} + \mathbf{x}_{o,j}^T \mathbf{u}_{o,i}) / 2 \text{ is the membrane strain,}$$

$$\varepsilon_{ij}^b = (\mathbf{x}_{o,i}^T \mathbf{u}_{n,j} + \mathbf{x}_{n,i}^T \mathbf{u}_{o,j} + \mathbf{x}_{o,j}^T \mathbf{u}_{n,i} + \mathbf{x}_{n,j}^T \mathbf{u}_{o,i}) / 2 \text{ is the bending strain.}$$

The conditions of rigid director $\mathbf{x}_n^T \mathbf{u}_n = 0$ and vanishing transverse shear strain $\varepsilon_{\zeta \zeta}^o = \varepsilon_{\zeta \eta}^o = 0$ yield:

$$\mathbf{u}_n = - \begin{bmatrix} \mathbf{x}_n^T \\ \mathbf{x}_{o,\zeta}^T \\ \mathbf{x}_{o,\eta}^T \end{bmatrix}^{-1} \begin{Bmatrix} 0 \\ \mathbf{x}_n^T \mathbf{u}_{o,\zeta} \\ \mathbf{x}_n^T \mathbf{u}_{o,\eta} \end{Bmatrix} = \frac{1}{j} [(-\mathbf{x}_{o,\eta} \times \mathbf{x}_n)(\mathbf{x}_n^T \mathbf{u}_{o,\zeta}) + (\mathbf{x}_{o,\zeta} \times \mathbf{x}_n)(\mathbf{x}_n^T \mathbf{u}_{o,\eta})]$$

which is orthogonal to \mathbf{x}_n . By making use of $\varepsilon_{\zeta i,j}^o = 0$ and the last equation,

$$\varepsilon_{ij}^b = -\mathbf{x}_n^T \mathbf{u}_{o,ij} - \mathbf{x}_{o,ij}^T \mathbf{u}_n = -\mathbf{x}_n^T \mathbf{u}_{o,ij} + \frac{1}{j} (\mathbf{x}_{o,ij} \times \mathbf{x}_{o,\eta})^T \mathbf{x}_n \mathbf{x}_n^T \mathbf{u}_{o,\zeta} - \frac{1}{j} (\mathbf{x}_{o,ij} \times \mathbf{x}_{o,\zeta})^T \mathbf{x}_n \mathbf{x}_n^T \mathbf{u}_{o,\eta}.$$

Let \mathbf{e}_1 and \mathbf{e}_2 be mutually perpendicular unit vectors tangential to \mathbf{x}_o , the vectors of physical membrane and bending strain components with respect to the \mathbf{e}_1 - and \mathbf{e}_2 -directions can be obtained as:

$$\begin{Bmatrix} \varepsilon_{11}^b \\ \varepsilon_{22}^b \\ 2\varepsilon_{12}^b \end{Bmatrix} = \mathbf{T} \begin{Bmatrix} \varepsilon_{\xi\xi}^b \\ \varepsilon_{\eta\eta}^b \\ 2\varepsilon_{\xi\eta}^b \end{Bmatrix}, \quad \begin{Bmatrix} \varepsilon_{11}^m \\ \varepsilon_{22}^m \\ 2\varepsilon_{12}^m \end{Bmatrix} = \mathbf{T} \begin{Bmatrix} \varepsilon_{\xi\xi}^m \\ \varepsilon_{\eta\eta}^m \\ 2\varepsilon_{\xi\eta}^m \end{Bmatrix}$$

where

$$\mathbf{T} = \begin{bmatrix} e_1^T x_{0,\zeta} e_1^T x_{0,\zeta} & e_2^T x_{0,\zeta} e_2^T x_{0,\zeta} & e_1^T x_{0,\zeta} e_2^T x_{0,\zeta} \\ e_1^T x_{0,\eta} e_1^T x_{0,\eta} & e_2^T x_{0,\eta} e_2^T x_{0,\eta} & e_1^T x_{0,\eta} e_2^T x_{0,\eta} \\ 2e_1^T x_{0,\zeta} e_1^T x_{0,\eta} & 2e_2^T x_{0,\zeta} e_2^T x_{0,\eta} & e_1^T x_{0,\zeta} e_2^T x_{0,\eta} + e_2^T x_{0,\zeta} e_1^T x_{0,\eta} \end{bmatrix}^{-1}.$$

References

- [1] B. Nayroles, G. Touzot, P. Villon, Generalizing the finite element method: diffuse approximation and diffuse elements, *Comput. Mech.* 10 (1992) 307–318.
- [2] T. Belytschko, Y.Y. Lu, L. Gu, Element-free Galerkin methods, *Internat. J. Numer. Methods Eng.* 37 (1994) 229–256.
- [3] W.K. Liu, S. Jun, Y.F. Zhang, Reproducing kernel particle methods, *Internat. J. Numer. Methods Eng.* 20 (1995) 1081–1106.
- [4] C.A.M. Duarte, J.T. Oden, A hp adaptive method using clouds, *Comput. Methods Appl. Mech. Eng.* 139 (1996) 237–262.
- [5] J.M. Melenk, I. Babuska, The partition of unity finite element method: basic theory and applications, *Comput. Methods Appl. Mech. Eng.* 139 (1996) 289–314.
- [6] S.N. Atluri, T. Zhu, A new meshless local Petrov–Galerkin (MLPG) method, *Comput. Mech.* 22 (1998) 117–127.
- [7] J.J. Monaghan, An introduction to SPH, *Comput. Phys. Commun.* 48 (1988) 89–96.
- [8] P.W. Randles, L.D. Libersky, Smoothed particle hydrodynamics: some recent improvements and applications, *Comput. Methods Appl. Mech. Eng.* 139 (1996) 375–408.
- [9] S.H. Park, S.K. Yoon, The least-squares meshfree method, *Internat. J. Numer. Methods Eng.* 52 (2001) 997–1012.
- [10] A. Bowyer, Computing Dirichlet tessellations, *Comput. J.* 24 (1981) 162–166.
- [11] S. Beissel, T. Belytschko, Nodal integration of the element-free Galerkin method, *Comput. Methods Appl. Mech. Eng.* 139 (1996) 49–74.
- [12] J. Bonet, S. Kulasegaram, Correction and stabilization of smooth particle hydrodynamics methods with applications in metal forming simulation, *Internat. J. Numer. Methods Eng.* 47 (1999) 1189–1214.
- [13] J.S. Chen, C.T. Wu, S. Yoon, Y. You, A stabilized conforming nodal integration for Galerkin mesh-free methods, *Internat. J. Numer. Methods Eng.* 50 (2001) 435–466.
- [14] J.S. Chen, S. Yoon, C.T. Wu, Non-linear version of stabilized conforming nodal integration for Galerkin mesh-free methods, *Internat. J. Numer. Methods Eng.* 53 (2002) 2587–2615.
- [15] Y. You, J.S. Chen, T.E. Voth, Characteristics of semi- and full-discretization of stabilized Galerkin meshfree method, *Finite Elements Anal. Design* 38 (2002) 999–1012.
- [16] P.G. Bergan, Finite elements based on energy orthogonal functions, *Internat. J. Numer. Methods Eng.* 15 (1980) 1541–1555.
- [17] C.A. Felippa, P.G. Bergan, A triangular element based on an energy-orthogonal free formulation, *Comput. Methods Appl. Mech. Eng.* 61 (1987) 129–160.
- [18] K.Y. Sze, Efficient formulation of robust hybrid elements using orthogonal stress/strain interpolants and admissible matrix formulation, *Internat. J. Numer. Methods Eng.* 35 (1992) 1–20.
- [19] T.H.H. Pian, P. Tong, Basis of finite elements for solids continua, *Internat. J. Numer. Methods Eng.* 1 (1969) 3–28.
- [20] T.H.H. Pian, State-of-the-art development of hybrid/mixed finite element method, *Finite Elements Anal. Design* 21 (1995) 5–20.
- [21] K.Y. Sze, C.L. Chow, An efficient hybrid stress quadrilateral Kirchhoff bending element, *Internat. J. Numer. Methods Eng.* 32 (1991) 149–169.